Nanoscale Advances

ROYAL SOCIETY OF CHEMISTRY

PAPER

View Article Online
View Journal

Cite this: DOI: 10.1039/d6na00177g

Ball milled magnetic sand as a dual-mode fluorescent sensor: turn-on detection of chlorpyrifos and turn-off response to glyphosate

Aaliya Qureashi,[ab] Arshid Bashir,[ac] Irfan Nazir,[ad] Zia ul Haq,[ae] Firdous Ahmad Ganaie,[a] Altaf Hussain Pandith[f] and Faheem A. Sheikh*[a]

Received 5th March 2026
Accepted 25th April 2026

DOI: 10.1039/d6na00177g

rsc.li/nanoscale-advances

The development of a low-cost fluorescent sensor material is of paramount importance for detecting persistent contaminants. We collected stones rich in iron near Magnetic Hill, Leh, India (34.171° N, 77.3525° E) and found them to be strongly fluorescent. We developed an intriguing, cost-effective fluorescent sensor based on ball-milled magnetic sand (BMMS) to detect two widely used organophosphorus pesticides, *e.g.*, glyphosate and chlorpyrifos. BMMS was systematically characterized by PXRD, XPS, TEM, SEM-EDX, and zeta potential measurements to confirm its structural, morphological, and surface properties. The sensor exhibited a fluorescence turn-off response to glyphosate and a turn-on response to chlorpyrifos, demonstrating selective interaction with the analytes. The detection limits (LOD) were determined to be 0.97 μM for glyphosate and 1.1 μM for chlorpyrifos. This fluorescence modulation is due to distinct molecular interactions with the surface Fe-based defect states. Furthermore, the practical applicability of BMMS was demonstrated using vegetable extracts, yielding excellent recovery rates of 92% to 100%. These findings underscore the potential of BMMS as a green, magnetically recoverable platform for pesticide monitoring in environmental and food samples.

1 Introduction

The extensive use and accumulation of organophosphorus pesticides, such as chlorpyrifos and glyphosate, have raised serious health and environmental concerns.[1] Although these pesticides are widely used in agriculture to eradicate weeds and pests, their excessive usage has been responsible for chronic toxicities in humans as well as animals, disrupting the ecosystem, particularly contaminating the soil and water.[2] Chloropyrifos, a neurotoxic chemical, inhibits acetylcholinesterase, an enzyme essential to nerve function.[3] Prolonged exposure to chlorpyrifos has been linked to endocrine failure, dementia, and developmental abnormalities, especially in pregnant women and children.[4] Several countries have limited and/or even banned chlorpyrifos usage because of its harmful effects on human health. Similarly, glyphosate, one of the most popular herbicides in the world, has sparked worries because of its potential carcinogenicity and disturbance of the gut microbiota.[5] Glyphosate, which the International Agency for Research on Cancer (IARC) has classified as "probably carcinogenic to humans," can also bind essential metal ions, which could have an impact on the availability of nutrients and the activities of enzymes in both plants and animals. Due to the presence of glyphosate residues in food, water, and human specimens, a worldwide debate has emerged about how to regulate and control its usage.[6,7] In modern times, significant technological and scientific innovations have greatly raised the quality of life. Still, they have contributed to rapid environmental degradation through increased industrialization, agricultural intensification, and human activities.[8,9]

To date, various conventional techniques, including AAS, ICP-MS, ICP-ES, HPLC, GC-MS, and X-ray fluorescence, have been widely employed for the detection of contaminants.[10–13] However, their dependence on complex instrumentation and limitations in selectivity and/or sensitivity have driven the exploration for alternative approaches.[14] In this context, fluorescence sensing has emerged as a promising technique due to its simplicity, high sensitivity, rapid response, and ability to enable simultaneous detection.[15–17] The surface chemistry, defect states, and the kinetics of interactions between the

[a]*Laboratory of Nanoscience and Quantum Computations, Department of Chemistry, University of Kashmir, Hazratbal, Srinagar, Jammu and Kashmir, 190006, India. E-mail: faheemnt@uok.edu.in*

[b]*Nanostructured and Biomimetic Lab, Department of Nanotechnology, University of Kashmir, Hazratbal, Srinagar, Jammu and Kashmir, 190006, India*

[c]*Department of Chemistry, Govt. Degree College, Beerwah, Budgam, Jammu and Kashmir, 193411, India*

[d]*National Institute of Technology, Hazratbal, Srinagar, Jammu and Kashmir, 190006, India*

[e]*The Institute of Technology, Zakura Campus, University of Kashmir, Jammu and Kashmir, 190006, India*

[f]*Lucent Institute of Excellence and Child Care, Sopore, Jammu and Kashmir, 193201, India. E-mail: altafpandit23@gmail.com*

sensing element and analytes all significantly influence the performance of sensing devices. Analyte adsorption and signal transduction are significantly enhanced by engineered surface flaws, oxygen vacancies, and heterostructured surfaces, according to recent developments in sensor materials. Specifically, research on advanced nanomaterials, such as CeO_2-decorated Y_2O_3 heterostructured nanosensors and $TbCrO_3$-based humidity sensors, has demonstrated the importance of active surface sites and interfacial interactions for improved sensitivity and selectivity.[18,19]

Over the years, numerous nanomaterials, including carbon dots, metal–organic frameworks, quantum dots, magnetite-based nanoparticles, and graphene-based composites, have been investigated for fluorescence sensing applications.[20–24] Nevertheless, frequent utilization of hazardous chemicals, multistep synthesis, and high production costs limit their applications.[25] A naturally occurring iron-rich mineral mostly composed of magnetite (Fe_3O_4) and other iron oxides and sulphides (*e.g.*, α-Fe_2O_3, $FeTiO_3$, and SiO_2), commonly referred to as magnetic sand, offers an unexplored and environmentally friendly resource for developing natural nanomaterials.[26,27] In contrast to synthetic nanoparticles, this sand is inherently magnetic due to the ferromagnetic properties of Fe_3O_4, making it readily accessible and environmentally benign. Because of its mineralogical composition, it can be used straight out of the ball mill without the need for doping and/or other chemical functionalization, which are standard procedures employed in the synthesis of conventional magnetite nanomaterials.[28]

Ball milling increases the surface area by decreasing particle size through continuous impact and attrition. It introduces oxygen-rich functional groups and surface defects, which collectively enhance magnetic response through quantum effects and improved domain alignment.[29] Such modifications provide active sites for analyte interaction in addition to improving its fluorescence properties. The resulting ball-milled magnetic sand (BMMS) exhibits tunable optical properties and becomes inherently fluorescent, making it a unique naturally occurring material.[30] In contrast to traditional fluorescent probes, which need hazardous precursors and produce toxic byproducts, BMMS offers a safe, economically viable alternative with single-step synthesis. Nevertheless, its inherent magnetic properties enable easy recovery and reuse, consistent with the growing focus on green chemistry. Furthermore, BMMS-based sensing procedures can eliminate the need for complex immobilization techniques and/or further functionalization, which greatly simplifies sensor production.[31–34]

Here, we present a new, environmentally friendly sensor based on BMMS that uses a fluorescence "on–off" mechanism to detect glyphosate and chlorpyrifos, respectively. The sand was processed to the nanoscale *via* facile ball milling, yielding surface imperfections and oxygenated groups that provide the material with intrinsic fluorescence. The magnetic characteristic enabled easy separation, making it reusable and environmentally friendly.

2 Experimental section

2.1. Materials and methods

Natural stones, which are known for magnetic properties, were collected in the vicinity of Magnetic Hill, Leh (India) (latitude

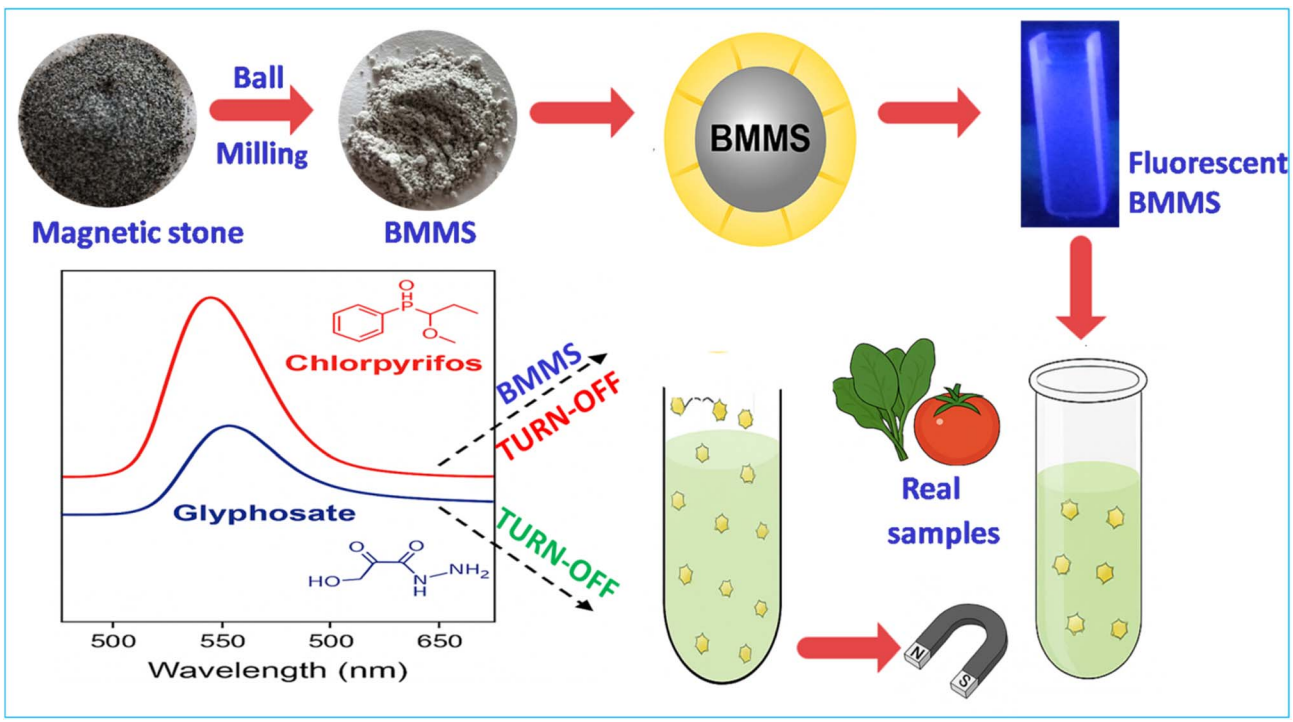

Scheme 1 Schematic illustration for the synthesis of BMMS and detection of chlorpyrifos and glyphosate.

34.171° N, and longitude 77.3525° E). The samples were thoroughly washed to remove unwanted mud and other surface impurities, then air-dried before being processed by high-energy ball milling for 24 hours. Glyphosate ($C_3H_8NO_5P$, purity >98%) and chlorpyrifos ($C_9H_{11}Cl_3NO_3PS$, purity >99%) were procured from Sigma-Aldrich for subsequent experimental procedures (Scheme 1).

2.2. Characterization of ball-milled magnetic sand (BMMS)

Fourier-transform infrared (FT-IR) spectra were recorded using a Bruker (α-12345390) spectrometer. The thermal stability of BMMS was evaluated using a simultaneous thermal analyzer (STA, LINSEIS, USA 6807/8835/16) over a temperature range of 20–800 °C at a heating rate of 10 °C min^{-1} under a nitrogen atmosphere. Surface morphology and elemental composition were characterized by scanning electron microscopy (SEM) equipped with EDS using a Zeiss Gemini SEM-500. High-resolution transmission electron microscopy (HR-TEM) was performed with a JEM-2010 microscope operating at 200 kV for visualization of atomic-scale structures of particles. Magnetic properties were measured using a vibrating sample magnetometer (Microsense E29). X-ray diffraction (XRD) analysis was performed on a Rigaku Ultima-IV diffractometer (Rigaku Corporation, Tokyo, Japan) using Cu Kα radiation ($\lambda = 1.5417$ Å). X-ray photoelectron spectroscopy (XPS) was conducted using a PHI 500 Versa Probe III to examine the surface chemical states of the BMMS. Surface charge measurements were carried out using an Anton Paar Litesizer 500 zeta potential analyzer.

2.3. UV-visible fluorescence properties

The optical properties of BMMS were examined using UV-visible absorption and fluorescence spectroscopy. UV-visible spectra were recorded using a Lasany LI-280 spectrophotometer over 200–800 nm, with BMMS dispersed in deionized water. Fluorescence emission spectra were obtained using a Shimadzu RF-5301 PC spectrofluorometer. The excitation-dependent fluorescence behaviour was studied by exciting the sample at various wavelengths (330–360 nm), and the emission was recorded in the visible range. All measurements were performed at room temperature (25 °C) using quartz cuvettes with a 1 cm path length.

2.4. Sensing protocol

Fluorescence responses were studied in aqueous medium upon following the sequential addition of chlorpyrifos and glyphosate. Detection limits (LOD) were determined following the 3σ/slope method.[35]

$$\mathrm{LOD} = 3 \times \frac{\text{standard deviation in experimental intensity values}}{\text{slope of intensity } \textit{vs.} \text{ concentration graph}} \quad (1)$$

2.5. Analysis of natural samples

The performance of the BMMS was evaluated using a spike/recovery approach to detect trace levels of pesticides in vegetable extracts. The extracts (*e.g.*, spinach and tomato) were prepared by blending, filtering, and centrifuging fresh samples. The unspiked extract was first analyzed using the BMMS-based fluorescence sensor. Known amounts (5 μM and 10 μM) of glyphosate and chlorpyrifos were then added to the same extract, and fluorescence intensity was measured after 10 minutes. Using the calibration curve, concentrations were determined, and recovery was calculated according to the protocol described elsewhere.[36]

$$\text{Recovery} = \frac{C_{\text{spiked}} - C_{\text{unspiked}}}{C_{\text{real}}} \times 100$$

3 Results and discussion

3.1. Morphological and structural characterization

Fourier transform infrared (FTIR) spectroscopy was first used to investigate the surface chemistry of ball-milled magnetic sand (BMMS). Moreover, some insights into the interaction mechanisms of glyphosate and chlorpyrifos with BMMS were corroborated, and the typical results are presented in the SI (Fig. S1). The FTIR data in Fig. S1 show spectra of pure magnetic sand. The spectra exhibited a strong absorption band around 3400 cm^{-1} corresponding to O–H stretching vibrations, indicating the presence of surface hydroxyl groups and/or adsorbed moisture. A relatively weak absorption peak around 2920 cm^{-1} corresponds to aliphatic C–H stretching. In contrast, the band around 1625 cm^{-1} was assigned to H–O–H bending vibrations, which further indicates the presence of water molecules and/or hydroxyl groups. Moreover, the presence of silica (SiO_2) content in BMMS is evidenced by a prominent strong absorption band within the range of 1040–1100 cm^{-1} corresponding to Si–O–Si stretching. A distinct band at 520 cm^{-1} is assigned to the presence of the Fe–O bond, indicating the presence of iron oxide phases.

The BMMS showed increased surface activity after ball milling, and its interaction with glyphosate was principally determined by the presence of hydroxyl (–OH), silanol (Si–OH), and iron oxide (Fe–O) groups. Glyphosate, which contains phosphonate ($-PO_3H_2$), carboxyl (–COOH), and amine ($-NH_2$) groups, interacts with BMMS predominantly through H-bonding and complexation mechanisms. The polar functional groups in glyphosate form strong hydrogen bonds with the surface-OH groups of the BMMS. In contrast, the negatively charged phosphonate groups bind to Fe^{3+} sites on BMMS, forming an inner-sphere complex *via* chelation. Evidence of glyphosate binding was confirmed by spectral shifts observed in the P–O stretching (1080–1140 cm^{-1}) and vibration band C=O/COO^- (~1590–1650 cm^{-1}).

Chlorpyrifos possesses phosphorothioate (P=S), phosphodiester (P=O), and aromatic functionalities, and interacts with BMMS through multiple mechanisms. These include moderate hydrogen bonding with surface hydroxyls, hydrophobic interactions arising due to its non-polar structure, and π–π stacking between chlorpyrifos aromatic rings and BMMS carbonaceous domains. Furthermore, small ligand-exchange pathways may exist between the phosphorus centres and the Fe sites on BMMS. The FTIR spectra indicate changes in aromatic C=C

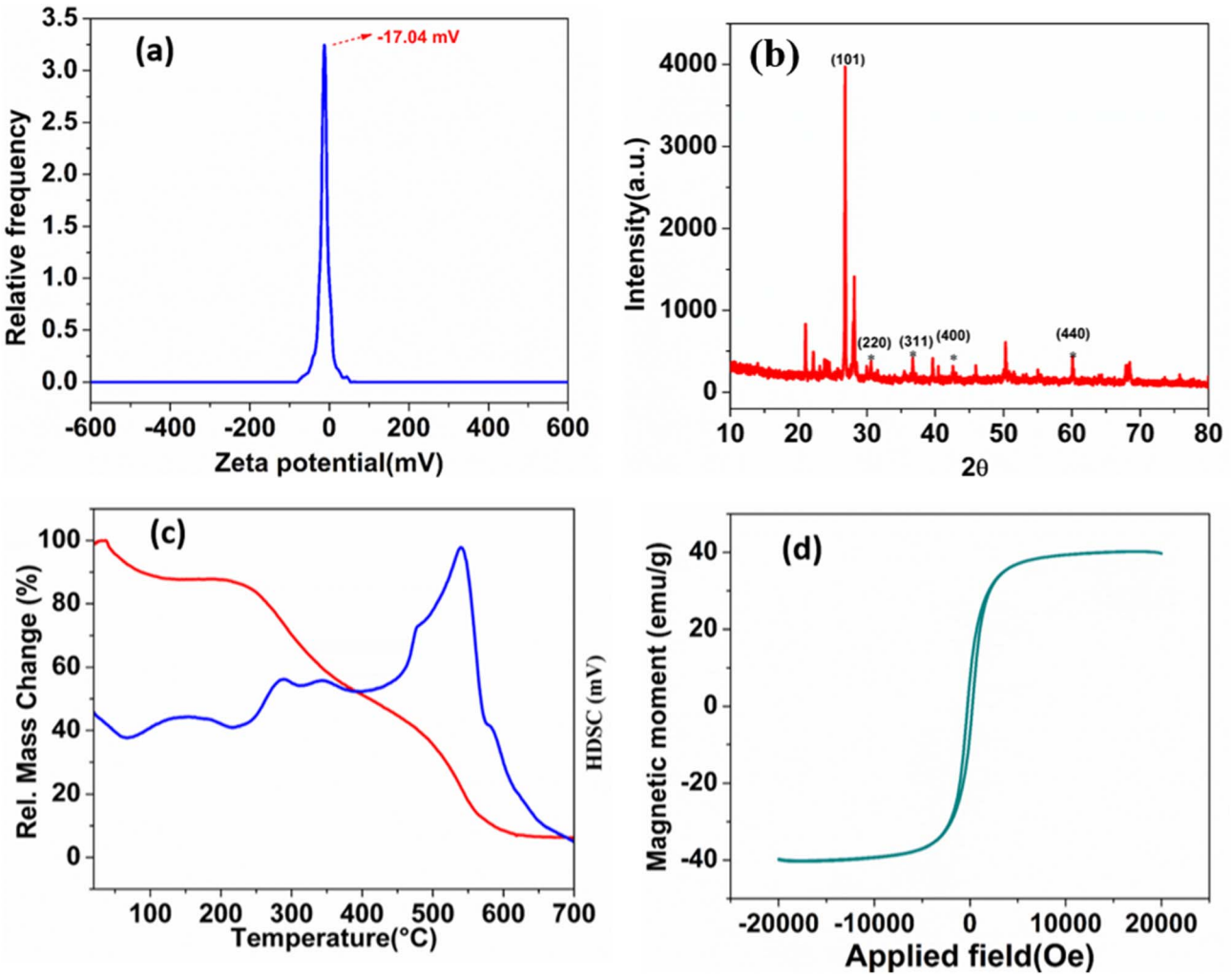

Fig. 1 (a) Zeta potential analysis in water. (b) XRD, (c) TGA, and (d) VSM analysis of BMMS.

(~1450–1600 cm^{-1}) and P═S/P–O (~850–1050 cm^{-1}) vibrations, indicating effective chlorpyrifos adsorption.

In line with this finding, zeta potential measurement of BMMS shows a negative charge of −17.04 mV, indicating moderate colloidal stability in aqueous solution (Fig. 1a). This negative charge prevents particles from adhering by promoting electrostatic repulsion, maintaining uniform dispersion, and enhancing solubility-like behavior in water. The observed stability aligns with FTIR studies, which confirm the presence of surface hydroxyl (–OH), silanol (Si–OH), and Fe–O groups. These functional groups not only contribute to the overall surface charge but also facilitate dispersion through hydrogen bonding and electrostatic repulsion. BMMS's stability and well-dispersed nature are critical for effective sensing interactions with glyphosate and chlorpyrifos.

Following the surface charge analysis, the structural analysis and phase composition of BMMS were investigated using X-ray diffraction (XRD). The BMMS sample reveals a broad range of diffraction peaks between 10° and 80° (2θ), indicating the polycrystalline nature of the material. Among these diffraction peaks, the most prominent is observed near 27.5°, corresponding to the (101) crystalline phase of quartz (SiO_2), suggesting its dominance (Fig. 1b). Several other peaks at $2\theta \approx$ 30.1°, 35.5°, 43.2°, 53.5°, and 57.0°, which are indexed to the (220), (311), (400), and (440) planes, respectively, do confirm the formation of a cubic spinel structure corresponding to magnetite (Fe_3O_4). The sharpness and intensity of these peaks imply that the ball-milling process, while reducing particle size, has retained the original crystallinity of the major phases. The presence of these magnetic and non-magnetic crystalline phases validates the composite nature of BMMS, making it a promising candidate for multifunctional environmental applications. This crystallinity is further supported by energy-dispersive X-ray spectroscopy (EDX) elemental mapping, which shows a uniform spatial distribution of key elements across the sample. The mapping image shows carbon (12%), nitrogen (10%), oxygen (17%), silicon (41%), and iron (20%), confirming the successful integration of magnetic and siliceous components, along with surface functional groups (Fig. S2).

Furthermore, the structural robustness of BMMS, as determined by XRD analysis, is supported by thermogravimetric analysis (TGA). The TGA curve (red) depicts the relative mass

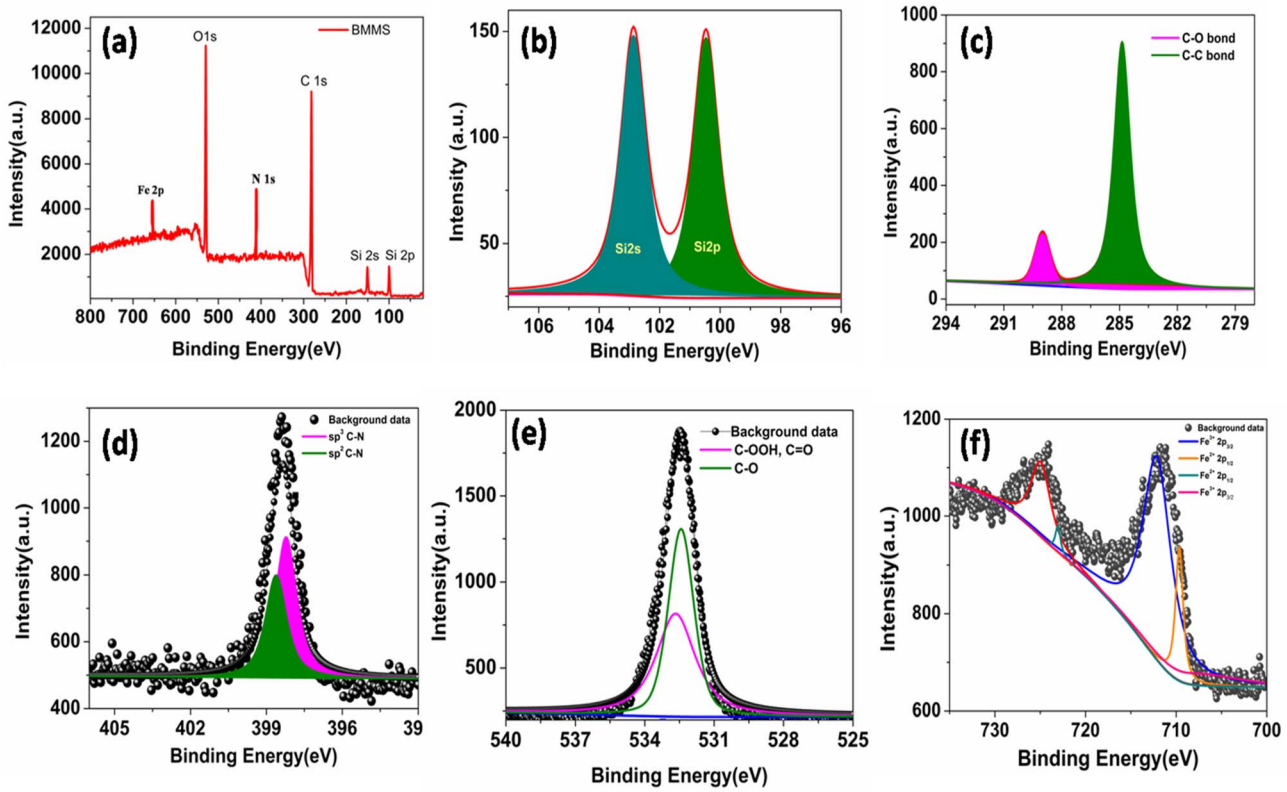

Fig. 2 (a) Complete surface scan (b) $Si_{2p,2s}$, (c) C_{1s}, (d) N_{1s}, (e) O_{1s}, and (f) Fe_{2p}.

change (%) as a function of temperature, and the blue curve corresponds to the differential scanning calorimetry (DSC) and/or differential thermal analysis (DTA) response (Fig. 1c). The TGA profile shows an initial mass loss below 200 °C, attributed to the evaporation of adsorbed water. A subsequent weight reduction occurs between 300 °C and 500 °C, likely due to the breakdown of organic moieties or surface-bound functional groups. A pronounced mass loss around 550–650 °C suggests structural degradation and phase transformation of the magnetic component, potentially involving the conversion of Fe_3O_4 to γ-Fe_2O_3 and/or α-Fe_2O_3. This is corroborated by the DSC/DTA curve, which displays an endothermic peak around 600 °C, supporting the occurrence of a phase transition or thermal decomposition event.

Moreover, the retention of magnetic behavior in BMMS after mechanical and thermal treatment was confirmed by vibrating sample magnetometry (VSM). The resulting S-shaped hysteresis loop is indicative of a ferromagnetic material, with a high saturation magnetization (M_s) of around 40 emu g^{-1} (Fig. 1d). The material also exhibits remanent magnetization (M_r) at zero field and a small coercivity (H_c), indicating soft magnetic behaviour. This confirms that the material retains good magnetic properties, making it suitable for magnetic separation and recovery applications. The combined TGA-DSC and VSM results demonstrate the thermal stability and strong ferromagnetic properties of BMMS, which are essential for environmental sensing or remediation applications.

Likewise, X-ray photoelectron spectroscopy (XPS) analysis of BMMS, as shown in Fig. 2, confirms the elemental composition and chemical states of the constituent elements. The survey spectrum (Fig. 2a) reveals prominent peaks corresponding to O_{1s}, Fe_{2p}, N_{1s}, C_{1s}, Si_{2p}, and Si_{2s}, confirming the presence of oxygen, iron, nitrogen, carbon, silicon, and other elements in the BMMS composite. The high-resolution Si_{2p} spectrum (Fig. 2b) shows two distinct peaks at ~103.3 eV and ~104.0 eV, attributed to $Si_{2p3/2}$ and $Si_{2p1/2}$, indicating the presence of silica. The C 1s spectrum (Fig. 2c) displays peaks at ~284.8 eV and ~288.5 eV, assigned to C–C and C=O bonds, respectively, suggesting surface functionalization. The N_{1s} spectrum (Fig. 2d) exhibits peaks at ~398.5 eV and ~400.3 eV corresponding to C–N and C=N bonds, implying nitrogen doping or amine functionalities. The O_{1s} spectrum (Fig. 2e) shows deconvoluted peaks at ~530.5 eV and ~532.8 eV, corresponding to metal–oxygen bonds and surface hydroxyl or carbonyl species. Finally, the Fe_{2p} spectrum (Fig. 2f) displays multiple peaks at ~710.5 eV and 724.0 eV, corresponding to $Fe_{2p3/2}$ and $Fe_{2p1/2}$, respectively, with accompanying satellite peaks. This confirms the presence of Fe^{3+} and Fe^{2+} oxidation states, indicative of magnetite-like structures. Altogether, this detailed XPS analysis validates the successful incorporation of magnetic, siliceous, and functionalized carbon-based components in BMMS.

SEM analysis reveals that the nanoparticles exhibit predominantly spherical to near-spherical morphologies with a range of sizes, resulting from strong impact forces and continuous attrition associated with high-energy mechanical ball milling. The process

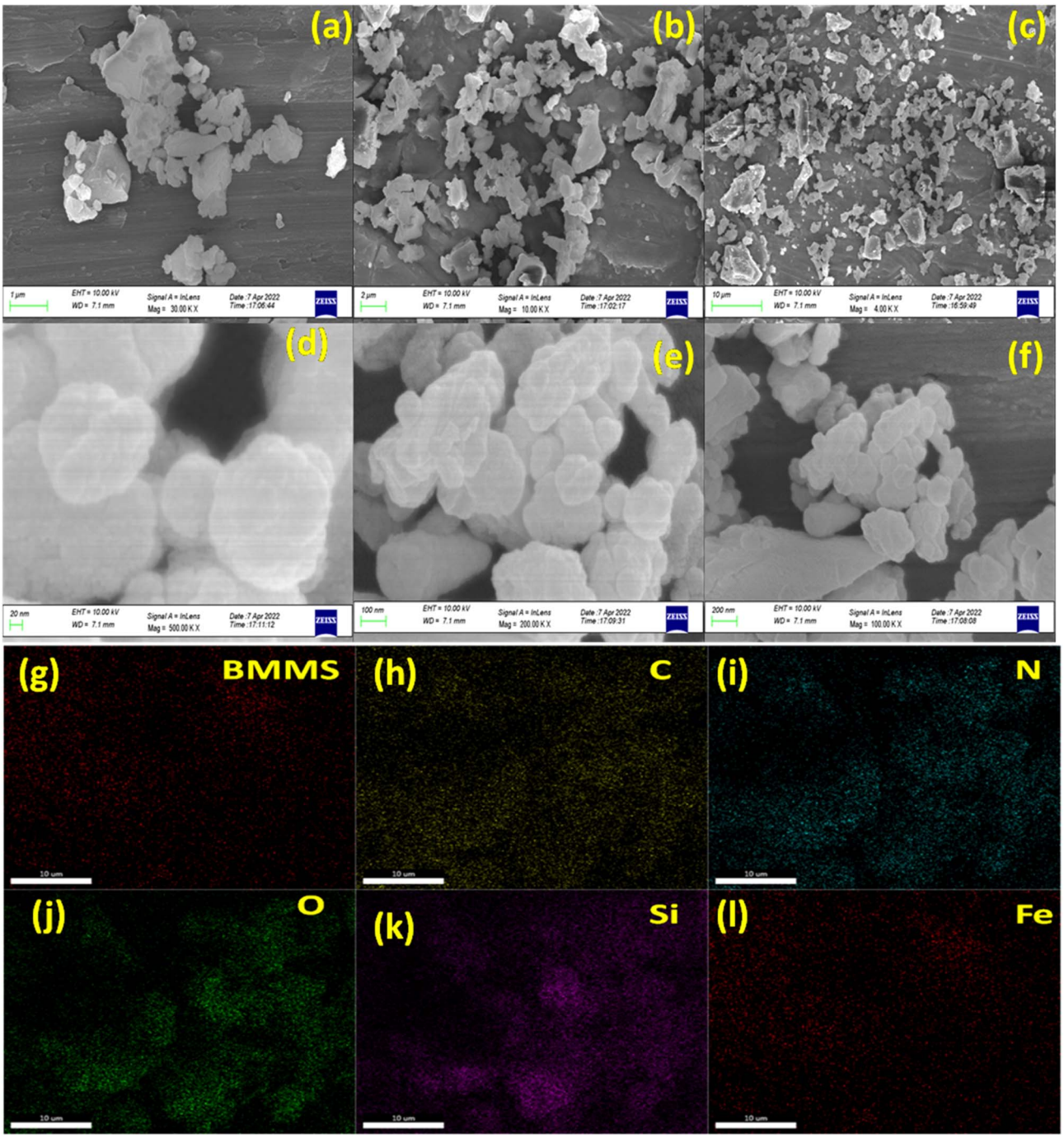

Fig. 3 FE-SEM micrographs (a–f) and mapping analysis (g–l) of BMMS.

effectively converts irregular rock fragments into more uniform and rounded structures. This morphology, resulting from repeated collisions and surface shearing during milling, enhances the surface area-to-volume ratio and promotes better dispersion in aqueous systems; an essential feature for adsorption and sensing applications (Fig. 3a–f).

The EDX elemental maps further confirm the homogeneous distribution of key elements—iron (Fe), silicon (Si), and oxygen (O)—across the BMMS surface (Fig. 3g–i). Fe signifies the magnetic phase, likely derived from naturally occurring magnetite and hematite, while Si and O originate from the siliceous matrix of the parent rock material. The even dispersion of Fe throughout the sample indicates successful milling without noticeable phase segregation, which is vital for achieving uniform magnetic behavior and reproducible sensing responses. The combined SEM-EDX analysis thus validates the structural integrity and compositional uniformity of BMMS, supporting its potential application in detecting environmental contaminants.

Furthermore, we captured TEM micrographs of BMMS at various magnifications to delve into their nanostructural

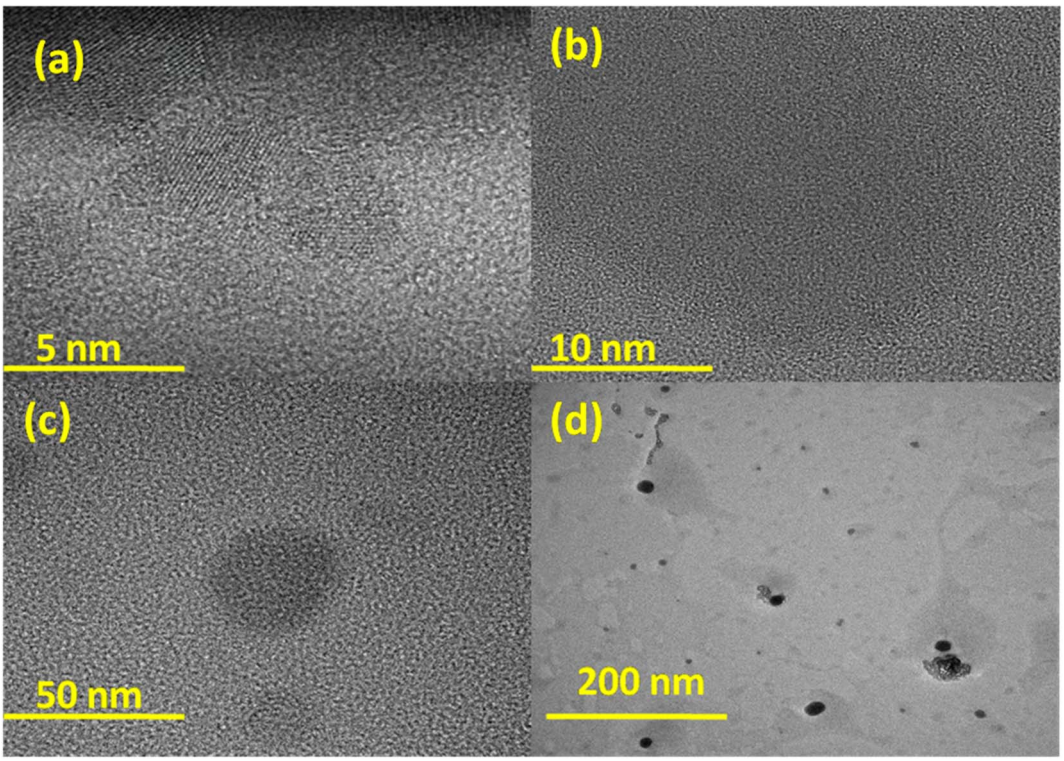

Fig. 4 (a–d) HR-TEM micrographs of ball-milled magnetite-silica (BMMS) nanoparticles at different magnifications: (a) 5 nm, (b) 10 nm, (c) 50 nm, and (d) 200 nm. The results reveal well-ordered atomic arrangement characteristic of magnetite (Fe_3O_4) and silica (SiO_2) phases.

features, as illustrated in Fig. 4a–d. At higher magnifications (5 nm and 10 nm), clear lattice fringes are observed, affirming the crystalline nature of the BMMS nanoparticles and indicating well-ordered atomic arrangements, typically associated with magnetite (Fe_3O_4) and silica (SiO_2) phases. At lower magnifications (50 nm and 200 nm), the TEM images reveal that the particles are nearly spherical to irregularly shaped, with sizes ranging from tens to hundreds of nanometers, and exhibit slight agglomeration, a common feature in magnetic materials due to dipole–dipole interactions. These results are consistent with the SEM images of the samples, confirming the nearly spherical morphologies. Furthermore, these observations align well with the XRD data, which confirm crystallinity, and the EDX elemental mapping, which demonstrates a homogeneous distribution of Fe and Si nanoparticles. Collectively, TEM analysis confirms the successful size reduction of ball-milled materials to nanoscale BMMS, characterized by well-defined crystalline structures and morphologies, making them suitable for surface-related applications such as sensing and adsorption.

3.2. Optical properties of BMMS: influence of solvent and time on fluorescence response

The optical characteristics of BMMS were examined through UV-visible absorption and fluorescence spectroscopy, as depicted in Fig. 5. In panel 5a, the UV-Vis absorption spectrum reveals a strong absorption below 300 nm, indicative of π–π^* transitions. These transitions likely arise from surface-adsorbed organic species or native functional groups present on the BMMS surface after ball milling. The presence of a shoulder peak at approximately 270 nm may be attributed to n–π^* transitions associated with oxygen-containing groups, suggesting partial surface oxidation or structural defects. Fig. 5b shows the fluorescence emission spectrum, which exhibits a sharp and intense peak centered at 525 nm, highlighting the ability of BMMS to emit visible fluorescence. This luminescent behavior is attributed to surface defect states or localized electronic transitions introduced during the high-energy ball milling process. Collectively, these observed optical characteristics suggest that BMMS holds promise as a cost-effective, magnetically recoverable fluorescent sensor material for detecting environmental contaminants.

The fluorescence behavior of BMMS was investigated in various solvents and over time to determine its optical stability and environmental responsiveness. In Fig. 5c, the emission intensity of BMMS varied significantly across solvents such as water, acetone, methanol, DMSO, and DMF. Among these, DMF exhibited the highest fluorescence intensity, which can be attributed to its strong polarity and solvation capacity that likely stabilize the surface states of BMMS, reduce non-radiative decay, and enhance radiative recombination. In contrast, lower intensities observed in water and methanol may result from hydrogen bonding-induced aggregation or fluorescence quenching. This suggests that solvent polarity and hydrogen-bonding ability play crucial roles in regulating the fluorescence of BMMS. Furthermore, Fig. 5d illustrates the temporal stability of BMMS, showing a noticeable increase in fluorescence intensity after 100 minutes compared to the initial

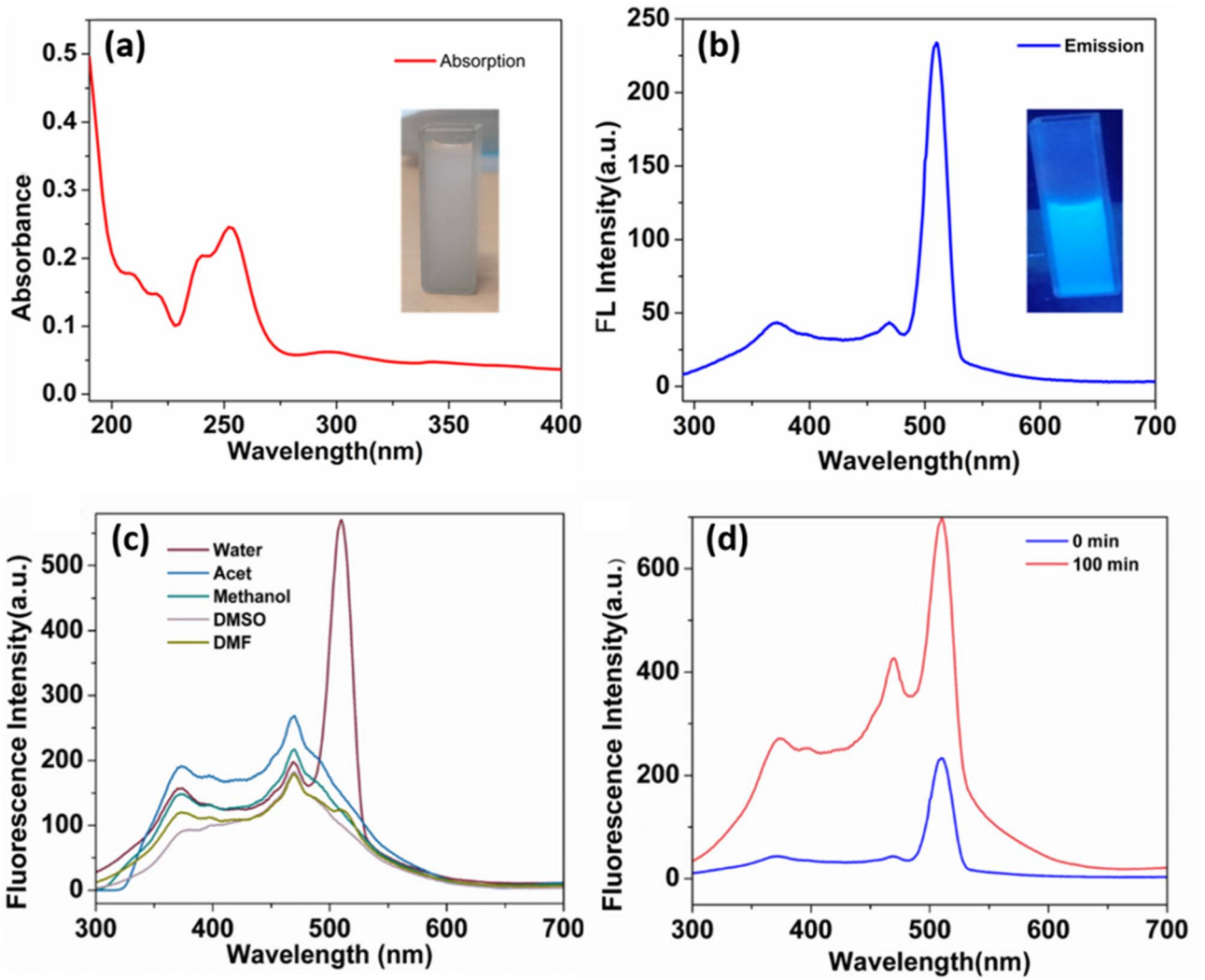

Fig. 5 (a) Absorption and (b) emission spectra of BMMS; (c) effect of using different solvents and (d) time on the fluorescence intensity of BMMS.

measurement. This enhancement is indicative of surface stabilization or delayed passivation effects that reduce non-radiative losses over time. The retention of spectral features over time confirms the structural and optical stability of BMMS, demonstrating its suitability for long-term applications in sensing and imaging.

3.3. Dual-mode fluorescence sensing of glyphosate and chlorpyrifos using BMMS

The fluorescence behaviour of BMMS was investigated in the presence of varying proportions of glyphosate, ranging from 2 to 25 μM. As illustrated in Fig. 6a, the fluorescence intensity of BMMS exhibited a remarkable quenching effect with increasing glyphosate concentration. The emission peaks, prominently observed in the 450–550 nm region, gradually decreased in intensity as glyphosate concentration increased. These findings highlight the strong interaction and possible electron or energy transfer between BMMS and glyphosate molecules.

A quantitative analysis was performed by plotting the fluorescence intensity ratio (F/F_o) against glyphosate concentration, where F and F_0 represent the fluorescence intensities in the presence and absence of glyphosate, respectively. In this regard, the Stern–Volmer plot (Fig. 6b) displayed a good linear relationship over the tested concentration range, following the equation $F/F_o = -0.0372$ [glyphosate] + 0.9723 with an R^2 value of 0.9864. The limit of detection (LOD) was calculated to be 0.97 μM, suggesting the high sensitivity of BMMS towards glyphosate. Notably, the calculated LOD falls below the maximum allowable concentration set by the U.S. Environmental Protection Agency (EPA) for glyphosate in drinking water. These results confirm the potential of BMMS as an effective, magnetically recoverable fluorescent probe, making it a promising candidate for glyphosate detection in environmental monitoring applications.

Similarly, the fluorescence response of BMMS to chlorpyrifos was investigated by monitoring its emission at increasing chlorpyrifos concentrations (2–25 μM). As shown in Fig. 6c, a distinct fluorescence enhancement was observed with rising chlorpyrifos levels, particularly around the 510 nm emission peak. This enhancement is likely due to the interaction of

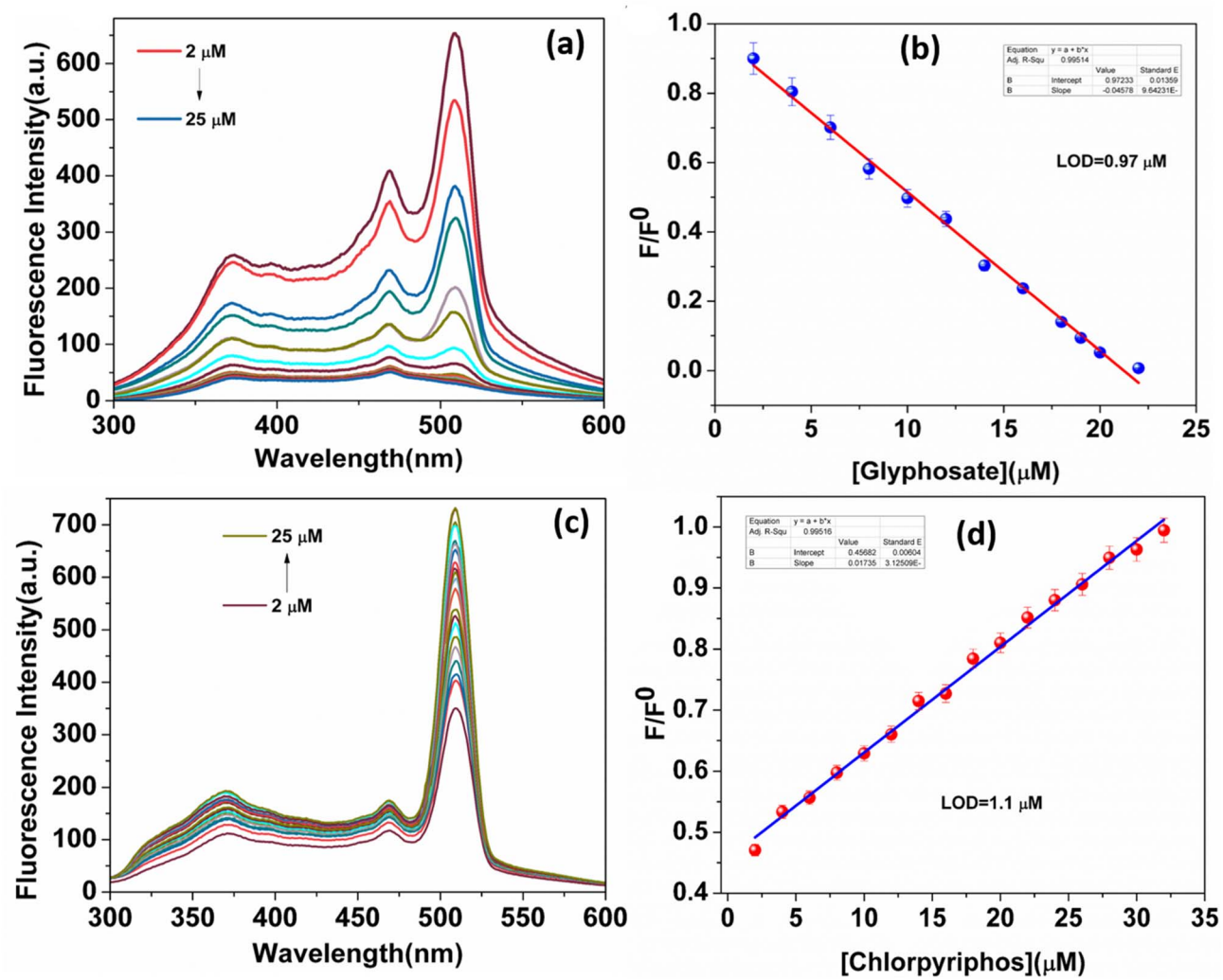

Fig. 6 (a) Effect of glyphosate on the FL intensity of BMMS, (b) Stern–Volmer plot showing the decrease in fluorescence intensity with increase in the concentration of glyphosate, (c) effect of chlorpyrifos on the fluorescence intensity of BMMS, (d) Stern–Volmer plot showing the increase in fluorescence intensity with increase in the concentration of chlorpyrifos.

chlorpyrifos molecules with the surface functional groups of BMMS, which may suppress non-radiative recombination pathways or induce structural rigidity, thereby increasing fluorescence intensity.

The graph showing the correlation between relative fluorescence intensity (F/F_0) and chlorpyrifos concentration is plotted in Fig. 6d. The results exhibited a good linear fit over the studied range. The calibration curve followed the equation $F/F_0 = 0.0189$ [chlorpyrifos] + 0.4588 with a high correlation coefficient ($R^2 = 0.9924$). The calculated LOD was 1.1 μM, demonstrating the potential of BMMS as a sensitive and selective fluorescence "turn-on" sensor for chlorpyrifos. The simplicity, reusability, and eco-friendly nature of BMMS underscore its promise for on-site detection of organophosphate pesticides in environmental samples.

The opposite fluorescence responses demonstrate the dual-mode sensing capability of BMMS. This enables selective and distinguishable detection of agrochemicals with varying

Table 1 Various materials that are used for glyphosate sensing

S. no	Material	Limit of detection (LOD)	References
1	Cu^{2+} modulated squaraine dye	13.16 n mol L^{-1}	37
2	Organo-probe (ZDA), synthesized by purine hydrazone derivative and 2,2′-dipyridylamine derivatives	11.6 nM	38
3	Antigen magnetic beads Fe_3O_4-GLY	8 ng mL^{-1}	39
4	Carbon dots	0.37 μM	40
5	Ball-milled magnetic sand (BMMS)	0.97 μM	This work

Table 2 Various materials used for chlorpyrifos sensing

S. no	Material	Limit of detection (LOD)	References
1	Oxime-functionalized carbazole	0.485 ppm	41
2	Eu(III)-8-allyl-3-carboxycoumarin probe	6.53 μM L^{-1}	42
3	9-Fluorenone oxime	15.5 μg L^{-1}	43
4	Magnetic Mn–ZnS molecularly imprinted probe (Fe_3O_4/Mn–ZnS/MIP)	0.41 ng mL^{-1}	44
5	Ball-milled magnetic sand (BMMS)	0.97 μM	This work

structural and functional characteristics. The differential interaction mechanisms—quenching *via* electron transfer in glyphosate and enhancement *via* restriction of non-radiative decay in chlorpyrifos—highlight the versatility of BMMS as a sustainable platform for pesticide monitoring in environmental matrices.

Furthermore, to demonstrate the novelty and performance of the present approach, comparisons with previously reported sensors for glyphosate and chlorpyrifos detection are presented in Tables 1 and 2, respectively. This comparison highlights its advantages in terms of practical application, selectivity, and sensitivity.

3.4. Probable mechanism

Based on the proposed mechanistic scheme, the fluorescence sensing behavior of BMMS toward glyphosate and chlorpyrifos can be explained through distinct interaction pathways. This leads to fluorescence quenching (turn-off) with glycophosphate and fluorescence enhancement (turn-on) with chlorpyrifos (Scheme 2).

In the presence of glyphosate, BMMS exhibits a fluorescence turn-off response. This is primarily due to glyphosate's ability to chelate with Fe^{3+} ions on the BMMS surface through its phosphonate ($-PO_3H_2$) and carboxyl (–COOH) functional groups. These groups form strong inner-sphere complexes with surface iron centres, effectively withdrawing electron density and disrupting the charge-transfer processes responsible for BMMS fluorescence. Additionally, hydrogen bonding and electrostatic interactions further stabilize the glyphosate–BMMS complex, leading to non-radiative decay pathways and quenching of the fluorescence signal.

In contrast, chlorpyrifos induces a fluorescence turn-on effect. This is attributed to weaker and more surface-localized interactions involving its phosphorothioate (P═S) group and aromatic ring system. The aromatic moiety of chlorpyrifos interacts *via* π–π stacking with carbonaceous domains on BMMS, and moderate hydrogen bonding with surface hydroxyl groups may also occur. These interactions stabilize the excited electronic state of BMMS and enhance radiative recombination, thereby increasing fluorescence intensity. Moreover, unlike

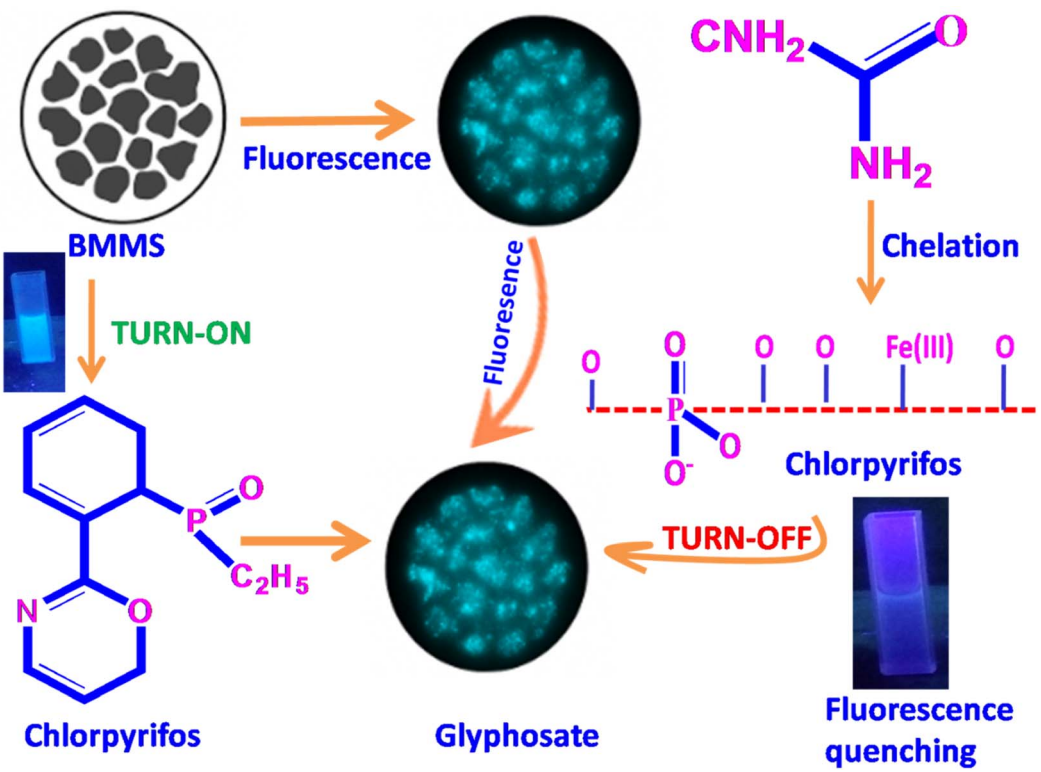

Scheme 2 Probable mechanism for the mode of interaction of BMMS with glyphosate and chlorpyrifos.

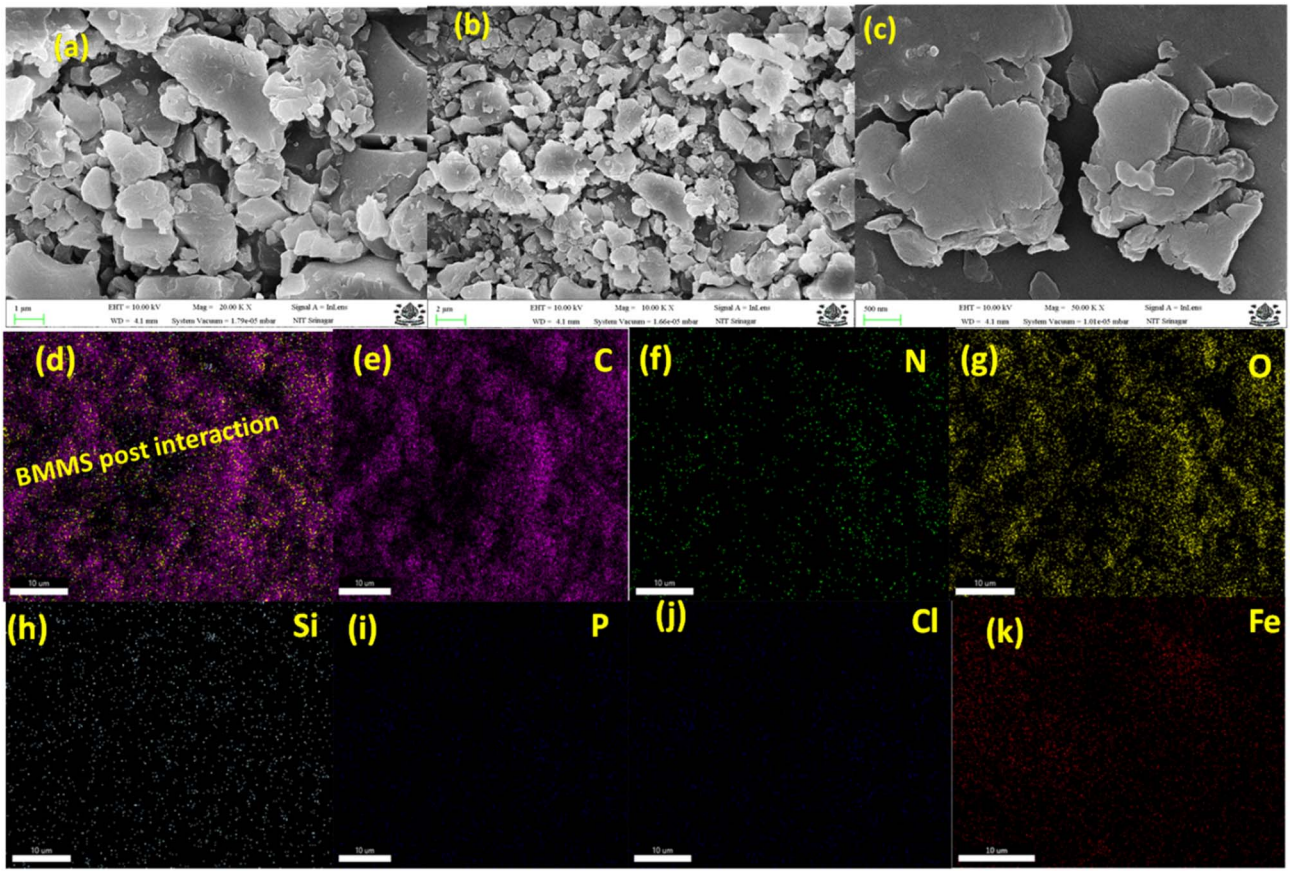

Fig. 7 (a–c) FE-SEM micrographs of BMMS and (d–k) elemental mapping analysis of BMMS after interaction with target analytes.

glyphosate, chlorpyrifos does not chelate Fe centers or introduce significant non-radiative pathways, allowing the emission signal to intensify. Thus, the dual fluorescence response of BMMS arises from the fundamental differences in the molecular structures and binding affinities of the two pesticides, enabling a selective turn-on/turn-off sensing platform for the detection of agrochemicals.

3.5. Post-interaction characterization of BMMS with pesticides

After exposure to chlorpyrifos and glyphosate, BMMS showed clear structural and surface changes. Post-adsorption SEM images (Fig. 7a–c) revealed that the initially rough, granular surface with well-dispersed particles became slightly smoother and more aggregated, indicating surface adsorption and partial coverage by pesticide molecules. Furthermore, elemental mapping (Fig. 7d–k) confirmed the uniform distribution of both pesticides on the BMMS surface. These morphological changes suggest strong interactions between BMMS active sites and pesticide molecules *via* hydrogen bonding, electrostatic forces, and π–π stacking. Despite these modifications, BMMS retained good colloidal stability, as shown by its moderately negative zeta potential, and preserved its magnetic properties (Fig. 8).

FTIR analysis supported these observations. After glyphosate adsorption, the O–H stretching band broadened and shifted, and new bands at 1230–1250 cm^{-1} appeared, corresponding to P═O or P–O vibrations of the phosphate group. These features indicate strong hydrogen bonding and surface passivation, consistent with the observed fluorescence quenching caused by non-radiative energy or charge transfer. In contrast, BMMS exposed to chlorpyrifos exhibited additional peaks at 1450–1500 cm^{-1} (aromatic C═C stretching) and stronger bands at 1230–1270 cm^{-1} (P═O and P–O–C vibrations), along with minor changes in Fe–O vibrations. These shifts point to surface-level physisorption and weaker electronic coupling. The electron-donating nature of chlorpyrifos likely promotes radiative recombination, explaining the enhanced fluorescence intensity. Overall, the SEM, elemental mapping, and FTIR results align with the fluorescence data: glyphosate quenches BMMS fluorescence, while chlorpyrifos enhances it. BMMS remains chemically and structurally robust after interaction with pesticides, confirming its suitability as a reusable material for environmental sensing applications.

Despite these interactions, BMMS maintained good colloidal stability as indicated by its moderately negative zeta potential, and its magnetic nature remained largely intact, confirming its structural robustness (Fig. 8).

3.6. Interference study

The selectivity of BMMS for glyphosate and chlorpyrifos was assessed in the presence of other agrochemical interferants. The characteristic fluorescence response for both analytes

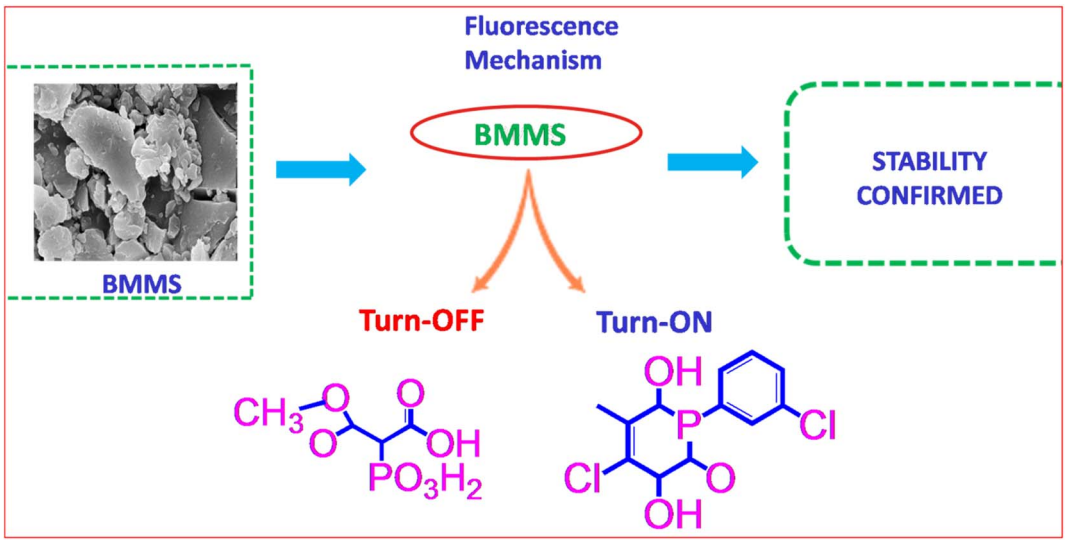

Fig. 8 Stability of BMMS post interaction with pesticides.

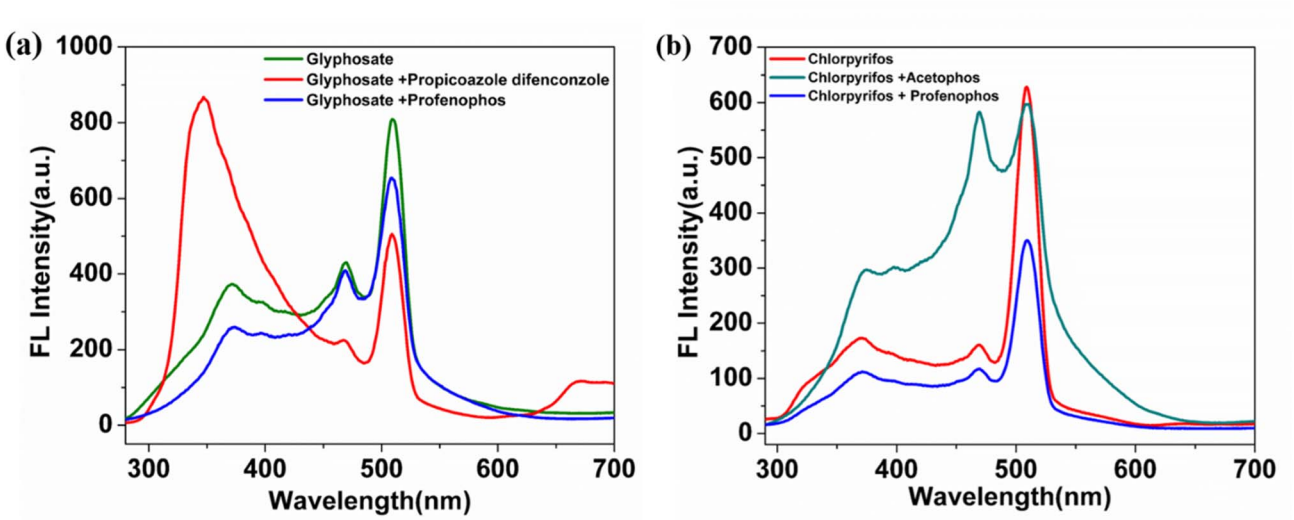

Fig. 9 Effect of potential interferents on the fluorescence intensity of (a) glyphosate and (b) chlorpyrifos.

remains essentially unaffected, with only minor changes in the intensity (Fig. 9a and b), demonstrating the sensitivity and selectivity of BMMS. The corresponding quantitative changes in fluorescence intensity in the presence of interferants are provided in the SI (Fig. S3a and b), further confirming the excellent anti-interference capability of the BMMS.

Table 3 Detection of glyphosate and chlorpyrifos in vegetable extracts using BMMS

Sample	Pesticide	Spiked (μM)	Unspiked (μM)	Measured (μM)	Recovery (%)
Spinach	Glyphosate	10	0.5	10.3	98.0
Tomato	Glyphosate	5	0.4	5.2	96.0
Spinach	Chlorpyrifos	10	0.6	10.5	99.0
Tomato	Chlorpyrifos	5	0.3	5.1	96.0

3.7. Real sample analysis

The BMMS-based fluorescence sensor was successfully applied to real vegetable extracts to assess its practical applicability. Recovery studies were performed by spiking spinach and tomato extracts with known concentrations (5 and 10 μM) of glyphosate and chlorpyrifos. The calculated recoveries ranged from 92% to 100%, indicating minimal matrix interference and high sensing accuracy (Table 3). These results confirm the suitability of the sensor for real-sample analysis, with excellent reliability and reproducibility.

4 Conclusion

In this work, we introduce a ball-milled magnetic sand (BMMS) derived from magnetic stones collected in the Ladakh Valley, India. The material exhibits distinctive fluorescence. The BMMS

exhibited an intriguing dual-mode fluorescence behavior in the presence of two well-known agrochemicals (chlorpyrifos and glyphosate). An on-off-on fluorescence sensing mechanism was well established, along with excellent sensitivity and stability of the material. The distinct fluorescence behavior towards each pesticide enables selective identification, while the good recovery rates from real vegetable samples (92–100%) affirm its applicability in real-world scenarios. This work highlights the promise of BMMS for environmental monitoring and food safety applications, owing to its green synthesis, magnetic recoverability, and robust sensing performance.

Conflicts of interest

The authors declare no conflict of interest.

Data availability

The data will be available on request.

Acknowledgements

AQ would like to acknowledge DST for providing a fellowship under the Women Scientist Scheme WOS-A (File No. CS-34/2021). We are also grateful to the Head of the Department of Chemistry at Kashmir University for providing the department with instrumentation facilities.

References

1 V. P. Kalyabina, El. N. Esimbekova, K. V. Kopylova and V. A. Kratasyuk, Pesticides: formulants, distribution pathways and effects on human health – a review, *Toxicol Rep*, 2021, **8**, 1179–1192.
2 J. Chen, T. M. J. A. Moerenhout, N. I. Kramer and I. M. C. M. Rietjens, Next Generation Risk Assessment of Acute Neurotoxicity from Organophosphate Exposures Using the In Vitro–In Silico Derived Dietary Comparator Ratio, *Environ. Sci. Technol.*, 2025, **59**(12), 6106–6114.
3 V. Terry, Functional consequences of repeated organophosphate exposure: Potential non-cholinergic mechanisms, *Pharmacol. Ther.*, 2012, **134**, 355–365.
4 Z. Arham and I. Ismaun, Electrochemical performance with a high synergy effect of chlorpyrifos pesticide sensor based on Al NPs doped TiO2-rich nanocomposite with the presence of C-dots as trapping agent, *Microchem. J.*, 2025, **212**, 113353.
5 J. Mazuryk, K. Klepacka, W. Kutner and P. S. Sharma, Glyphosate: Hepatotoxicity, Nephrotoxicity, Hemotoxicity, Carcinogenicity, and Clinical Cases of Endocrine, Reproductive, Cardiovascular, and Pulmonary System Intoxication, *ACS Pharmacol. Transl. Sci.*, 2024, **7**(5), 1205–1236.
6 A. Qureashi, A. H. Pandith, A. Bashir, L. A. Malik, T. Manzoor, F. A. Sheikh, K. Fatima and Z. ul Haq, Electrochemical analysis of glyphosate using porous biochar surface corrosive nZVI nanoparticles, *Nanoscale Adv.*, 2023, **5**, 742–755.
7 C. Bou-Mitri, S. Dagher, A. Makkawi, Z. Khreyss and H. F. Hassan, Glyphosate in food: A narrative review, *J. Agric. Food Res.*, 2025, **19**, 101643, DOI: 10.1016/j.jafr.2025.101643.
8 R. Das, S. Das, P. P. Phukan, S. Shaheen, K. S. Kakati, D. Borbora, T. Ahmad and A. Baruah, WS2-integrated TiO2/Soot: A Novel Multifunctional Nanocomposite for Synergistic Dye Degradation, Photocatalytic Hydrogen Evolution and Antibacterial Applications, *Surf. Interfaces*, 2025, **74**, 107710.
9 N. A. Pandit, I. Sadiq, S. M. Alshehri, S. A. Ali and T. Ahmad, Designing of Advanced ZrO2-Y2O3 pn Heterojunction for Efficient Carbon Monoxide Gas Sensing, *Ceram. Int.*, 2025, **51**, 52486–52494.
10 M. Jin, H. Yuan, B. Liu, J. Peng, L. Xu and D. Yang, Review of the distribution and detection methods of heavy metals in the environment, *Anal. Methods*, 2020, **12**(48), 5747–5766.
11 Y. Bai, Y. Zhang, X. Liu, *et al.*, The spatial distribution and source apportionment of heavy metals in soil of Shizuishan, China, *Environ. Earth Sci.*, 2023, **82**, 494, DOI: 10.1007/s12665-023-11192-8.
12 P. Zhang, L. Hu, B. Gao, F. Gao, X. Zhu, Y. Li and H. Yao, Spatial-temporal variation and source analysis of heavy metals in different land use types in Beilun District (2015 and 2022), *Sci. Rep.*, 2024, **14**(1), 15127, DOI: 10.1038/s41598-024-65811-w.
13 P. Rai, A. Majumdar and S. Basu, Recent Trends in Nanomaterials-Based Sensing of Environmental Contaminants, *Microchem. J.*, 2020, **156**, 104831.
14 B. H. Abdelmonem, L. T. Kamal, R. M. Elbaz, M. R. Khalifa and A. Abdelnaser, From contamination to detection: The growing threat of heavy metals, *Heliyon*, 2025, **11**, e41713.
15 J. Tian, M. An, X. Zhao, Y. Wang and M. Hasan, Advances in Fluorescent Sensing Carbon Dots: An Account of Food Analysis, *ACS Omega*, 2023, **8**(10), 9031–9039.
16 A. Qureashi, A. H. Pandith, A. Bashir and L. A. Malik, Biomass-derived carbon quantum dots: a novel and sustainable fluorescent "ON–OFF–ON" sensor for ferric ions, *Anal. Methods*, 2021, **13**, 4756–4766.
17 N. A. Pandit, S. M. Alshehri, S. A. Ali and T. Ahmad, Chemo-Resistive CeO2-Decorated Y2O3 Heterostructured Nanosensors for Selective Ammonia Detection, *Chem. Nanostruct. Mater.*, 2026, **12**, e202500293.
18 H. Lone, T. Islam, J. Ahmed, S. Ahmed, K. V. Ramanujachary and T. Ahmad, Highly Sensitive TbCrO3 Capacitive Humidity Nanosensor Prepared by Sol–Gel Combustion, *ChemistrySelect*, 2025, **10**, e202403566.
19 S. Huang, P. Mu, G. Li, W. Ni, Y. Fang, F. Wei and Q. Xiao, Highly sensitive red-emitting carbon dot-based fluorescence sensor for simultaneous detection of copper ions and L-histidine in environmental and biomedical samples, *J. Photochem. Photobiol., A*, 2025, 116588, DOI: 10.1016/j.jphotochem.2025.116588.
20 A. M. B. H. Ali, M. R. Elmasry, Y. A. B. Jardan and M. M. El-Wekil, Smart fluorometric sensing of metal contaminants in canned foods: a carbon dot-based dual-response system for quantifying aluminum and cobalt ions, *RSC Adv.*, 2025, **15**, 6962–6973.

21 Y. Jiang, C. Wenxin, L. Zhihao, Z. Xiang, Z. Panjing, H. Xuehai, P. Xinyi, H. Zhenda, Y. Wang and T. Zhongqun, Synergistic Aggregation-Induced Emissive Linkers in Metal–Organic Frameworks for Ultrasensitive and Quantitative Visual Sensing, *JACS Au*, 2025, **5**(4), 1875–1883.

22 C. E. Enyoh, Q. Wang, W. Wang, M. Suzuki, G. Masuda, D. Nakajima and S. Lu, Green One-Step Synthesis and Characterization of Fluorescent Carbon Quantum Dots from PET Waste as a Dual-Mode Sensing Probe for Pd (II), Ciprofloxacin, and Fluoxetine *via* Fluorescence Quenching and Enhancement Mechanisms, *Surfaces*, 2025, **8**, 24.

23 N. Senthilnathan, C. M. Oral and M. Pumera, Magneto-fluorescent microrobots with selective detection intelligence for high-energy explosives and antibiotics in aqueous environments, *ACS Appl. Mater. Interfaces*, 2025, **17**, 21691–21704.

24 A. Mohanty, S. Upadhye, G. K. Pradhan and P. Nayak, Ultrasensitive detection of arsenic in water using laser-scribed graphene-based electrodes, *J. Mater. Chem. B*, 2025, **13**, 7393–7400.

25 K. Patra, S. Dey, C. Solanki, A. Sengupta and V. K. Mittal, Harnessing Advanced Porous Materials, Covalent Organic Frameworks, and Porous Organic Polymers as Next-Generation Porous Frameworks for Targeted Removal of Emerging Water Contaminants, *ACS Appl. Eng. Mater.*, 2025, **3**, 1130–1165.

26 A. Qureashi, Z. u. Haq, A. Bashir, I. Nazir, F. A. Ganaie, K. Fatima, L. A. Malik, F. A. Sheikh and A. H. Pandith, Bifunctional Zirconium Phosphate with Greigite for Electrochemical Detection and Simultaneous Removal of Heavy Metal Ions and Nitro Compounds, *Langmuir*, 2024, **40**(28), 14486–14503.

27 A. Bashir, A. H. Pandith, A. Qureashi and L. A. Malik, Fe_3S_4 nanoparticles wrapped in a gC_3N_4 matrix: an outstanding visible active Fenton catalysis and electrochemical sensing platform for lead and uranyl ions, *New J. Chem.*, 2023, **47**, 1548–1562.

28 D. Raabe, The Materials Science behind Sustainable Metals and Alloys, *Chem. Rev.*, 2023, **123**(5), 2436–2608.

29 R. Zheng, L. Zhu, C. Li, Z. Wu, Y. Huang, J. Yang, R. Wei, X. Zhu and Y. Sun, Ball milling as an effective method for improving oxygen evolution reaction electrocatalyst Ca3Co4O9, *J. Electroanal. Chem.*, 2023, **931**, 117182, DOI: 10.1016/j.jelechem.2023.117182.

30 W. A. Ali, S. E. Richards and R. H. Alzard, Unlocking the potential of ball milling for nanomaterial Synthesis: An overview, *J. Ind. Eng. Chem.*, 2025, **149**, 63–93, DOI: 10.1016/j.jiec.2025.01.054.

31 J. P. Lange, Managing Plastic Waste-Sorting, Recycling, Disposal, and Product Redesign, *ACS Sustainable Chem. Eng.*, 2021, **9**(47), 15722–15738.

32 A. Taufiq, S. l Bahtiar, R. E. Saputro, D. Yuliantika, A. Hidayat, S. Sunaryono, N. Hidayat, S. Samian and S. Soontaranon, Fabrication of Mn1-xZnxFe2O4 ferrofluids from natural sand for magnetic sensors and radar absorbing materials, *Heliyon*, 2020, **6**, e04577, DOI: 10.1016/j.heliyon.2020.e04577.

33 M. Hamed, M. A. E. Aal, M. A. Khaled, S. M. Ghoneim, E. Saad, J. Seong Lee and A. E. D. H. Sayed, Occurrence, distribution, and composition of black sand along the Red Sea, Egypt, *Sci. Total Environ.*, 2024, **923**, 171277, DOI: 10.1016/j.scitotenv.2024.171277.

34 A. Taufiq, A. Nikmah, A. Hidayat, S. Sunaryono, N. Mufti, N. Hidayat and H. Susanto, Synthesis of magnetite/silica nanocomposites from natural sand to create a drug delivery vehicle, *Heliyon*, 2020, **6**, e03784.

35 Z. U. Haq, F. A. Ganaie, S. A. Bhat, I. Nazir, A. Qureashi, A. Bashir and M. A. Rizvi, Integrating 2D graphitic carbon nitride with Gd 2 S 3 nanoparticles towards development of multiutility water treatment nanomaterial: synergistic effects on electrochemical dopamine sensing and photocatalytic degradation of contaminants, *New J. Chem.*, 2024, **48**, 16461–16474.

36 I. Nazir, A. Qureashi, A. Bashir, Z. U. Haq, F. A. Ganaie, G. N. Dar and A. H. Pandith, Synergistic Sb2S3-NiS2 heterostructure: A robust electrocatalyst for electrochemical sensing of Hg (II), As (III) ions and carbendazim fungicide, *J. Environ. Chem. Eng.*, 2024, **12**, 112793.

37 S. Zhao, L. Shi, X. Zhang, X. Sun, W. Zhu and L. Yu, An on–off–on fluorescent probe for the detection of glyphosate based on a Cu^{2+}-assisted squaraine dye sensor, *Anal. Methods*, 2024, **16**, 1341–1346.

38 X. Tao, Y. Mao, S. Alam, A. Wang, X. Qi, S. Zheng, C. Jiang, S. Y. Chen and H. Lu, Sensitive fluorescence detection of glyphosate and glufosinate ammonium pesticides by purine-hydrazone-Cu^{2+} complex, *Spectrochim. Acta, Part A*, 2024, **314**, 124226.

39 D. Wang, B. Lin, Y. Cao, M. Guo and Y. Yu, A Highly Selective and Sensitive Fluorescence Detection Method of Glyphosate Based on an Immune Reaction Strategy of Carbon Dot Labeled Antibody and Antigen Magnetic Beads, *J. Agric. Food Chem.*, 2016, **64**(30), 6042–6050.

40 G. F. Barreto, R. Mathias, O. Fabiano and V. Pereira, Carbon Dots-Based Fluorescent Sensor for Glyphosate Detection *via* Fe^{3+}-Mediated Fluorescence Quenching and Recovery, *ACS Omega*, 2025, **10**(49), 60844–60858.

41 P. Thadatontichok, C. Pinthong, N. Kaewnok, J. Sirirak, N. Thepsuparungsikul, N. Wanichacheva and K. Setthakarn, Novel Dual-Mode Fluorescent Sensor for Detecting Chlorpyrifos and Cu(II), *ACS Omega*, 2025, **10**, 29732–29740.

42 H. A. Azab, G. M. Khairy and R. M. Kamel, Time-resolved fluorescence sensing of pesticides chlorpyrifos, crotoxyphos and endosulfan by the luminescent Eu(III)–8-allyl-3-carboxycoumarin probe, *Spectrochim. Acta, Part A*, 2015, **148**, 114–124.

43 E. Donà and A. Lobnik, Chlorpyrifos Detection Based on 9-Fluorenone Oxime, *Chemosensors*, 2025, **13**, 170.

44 S. Kumar, S. Bhogal, G. Kaur, A. K. Malik and J. S. Aulakh, Turn-off fluorescent magnetic Mn-ZnS molecularly imprinted probe for the detection of chlorpyrifos in vegetable samples, *Spectrochim. Acta, Part A*, 2025, **330**, 125623.

